Selective accumulation of matrix proteins inside of peroxisomal subdomains

Julia Ast[1,2*], Nils Bäcker[1*], Domenica Martorana[1*], Christian Renicke[1,3], Thorsten Stehlik[1], Thomas Heimerl[4,5], Christof Taxis[1,6], Gert Bange[4,5], Michael Bölker[1,5], Björn Sandrock[1], Kay Oliver Schink[7,8§] and Johannes Freitag[1§]

1 Department of Biology, Philipps-University Marburg, Marburg, Germany

2 Institute of Metabolism and Systems Research (IMSR), and Centre of Membrane Proteins and Receptors (COMPARE), University of Birmingham, Birmingham, United Kingdom

3 Department of Genetics, Stanford University School of Medicine, Stanford, CA, USA.

4 Department of Chemistry, Philipps-University Marburg, Marburg, Germany

5 Center for Synthetic Microbiology (SYNMIKRO), Philipps-University Marburg, Marburg, Germany

6 School of Life Sciences, University of Siegen, Siegen, Germany

7 Centre for Cancer Cell Reprogramming, Faculty of Medicine, University of Oslo, Montebello, Oslo, Norway

8 Department of Molecular Cell Biology, Institute for Cancer Research, Oslo University Hospital, Montebello, Oslo, Norway

[*] these authors contributed equally

[§] to whom correspondence should be addressed:

k.o.schink@medisin.uio.no

johannes.freitag@biologie.uni-marburg.de

Abstract

Formation of specialized reaction spaces prevents interference between distinct cellular pathways. Peroxisomes are cellular compartments involved in a large diversity of metabolic processes. How peroxisomes differentiate into subpopulations and by which mechanism intraorganellar domains are formed remains largely elusive. Here, we report on enzymes from the fungus *Ustilago maydis*, which accumulate inside of peroxisomal subdomains. We describe a short peptide motif (Tyr-Ile-Ile-Val) sufficient to trigger focal localization. Mining for proteins with similar motifs uncovered several peroxisomal matrix proteins that accumulate in intraorganellar foci. These foci are enriched in the enzyme urate oxidase – a typical constituent of the paracrystalline core of peroxisomes. Upon peroxisome proliferation uneven distribution of focal structures results in the formation of peroxisome subpopulations with different protein content. The underlying principle of subdomain formation is evolutionary conserved in mammalian peroxisomes and formation of similar foci was also observed inside of mitochondria. We propose that peroxisomal proteins show an individual propensity to self-assemble. This formation of protein aggregates appears to be a ubiquitous driving force to spatially organize the peroxisomal proteome.

37 **Introduction**

38 Peroxisomes are cellular compartments surrounded by a single membrane. They contain many
39 metabolic enzymes, in particular those required for degradation of fatty acids and detoxification
40 of hydrogen peroxide (Poirier et al., 2006; Smith and Aitchison, 2013). In humans, peroxisomes
41 are essential and mutation of peroxisomal biogenesis proteins (Peroxins or Pex proteins) leads
42 to severe disorders including the Zellweger syndrome (Wanders, 2014). Import of proteins into
43 the matrix of peroxisomes requires either of two cytosolic targeting factors, Pex5 and Pex7
44 (Francisco et al., 2017; Kim and Hettema, 2015). They recognize specific sequence motifs
45 located either at the Carboxy (*C*)-terminal end of the cargo protein (peroxisomal targeting signal
46 type 1; PTS1) or within the Amino (*N*)-terminal part (peroxisomal targeting signal type 2;
47 PTS2) (Lazarow, 2006; Walter and Erdmann, 2019). The prototype PTS1 bound by Pex5 is a
48 tripeptide with the amino acid sequence Ser-Lys-Leu (Gould et al., 1989).

49 Fungal peroxisomes are diverse and contain specialized metabolic pathways e.g. for secondary
50 metabolite and siderophore biosynthesis, methanol degradation and carbohydrate metabolism
51 (Bartoszewska et al., 2011; Freitag et al., 2012; Gründlinger et al., 2013; Stehlik et al., 2014;
52 van der Klei and Veenhuis, 2006). A peculiar variant of peroxisomes identified in *Neurospora*
53 *crassa* are Woronin bodies, which seal septal pores in wounded hypha (Jedd and Chua, 2000;
54 Nguyen et al., 2021). Differentiation of peroxisomes into Woronin bodies is achieved through
55 expression of the Hex1 protein, which forms large crystals in Woronin bodies and is their major
56 constituent (Pieuchot and Jedd, 2012; Tey et al., 2005).

57 The mechanisms by which peroxisomes differentiate into subpopulations in other biological
58 systems or how they form intraorganellar domains are largely uncharacterized. Isolation and
59 biochemical characterization of rat liver peroxisomes revealed peroxisomal populations with
60 different protein content (Völkl et al., 1999). In yeast, distinct peroxisome populations can be
61 distinguished by means of their age (Kumar et al., 2018). In plants, different types of
62 peroxisomes emerge during development (Hu et al., 2012; Lingard et al., 2009). High-
63 resolution imaging studies uncovered the presence of subdomains inside of the peroxisomal
64 membrane of the yeast *Saccharomyces cerevisiae* (Galiani et al., 2016). Early electron
65 microscopy and biochemical studies demonstrated that the enzyme urate oxidase is a major
66 constituent of an electron-dense paracrystalline core structure (Rouiller & Bernard, 1956; De
67 Duve, 1960; Baudhuin et al, 1965; De Duve & Baudhuin, 1966; Völkl et al, 1988).

68 Here we show, that a short peptide motif drives the accumulation of peroxisomal matrix
69 proteins into subdomains, which we propose to be related to the electron-dense paracrystalline

70 core. Focal accumulation determines both the protein distribution within single peroxisomes
71 and the formation of peroxisomes with different protein content upon organelle proliferation.
72
73 **Results**
74 **Identification of peroxisome subpopulations in *U. maydis***
75 We have previously shown that in *U. maydis* the acyltransferases, Mac1 and Mac3, involved in
76 biosynthesis of surface-active mannosylerythritol lipids (MELs), are localized to peroxisomes
77 (Becker et al., 2021; Bölker et al., 2008; Freitag et al., 2014; Kämper et al., 2006). Upon a
78 closer inspection of fluorescence microscopic images we noticed that both enzymes are not
79 homogenously distributed among the entire population of peroxisomes (Fig. 1A).
80

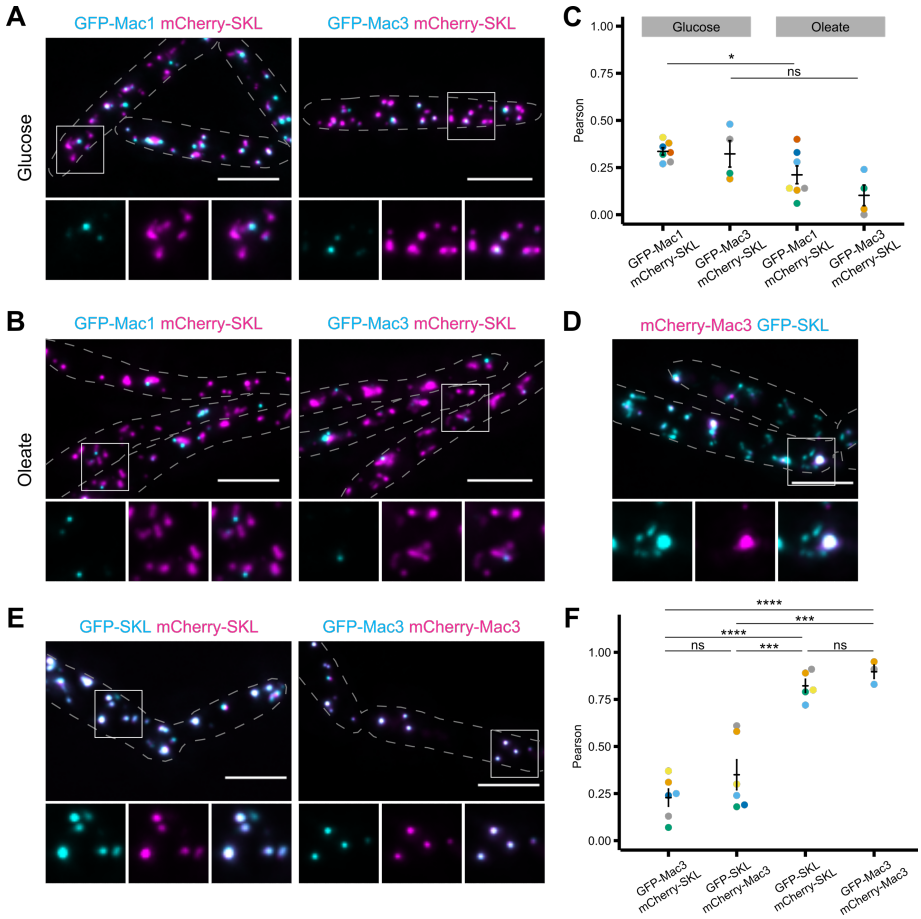

81
82 **Figure 1 Acyltransferases Mac1 and Mac3 accumulate in peroxisome subpopulations**
83 *U. maydis* strains expressing N-terminally GFP-tagged versions of Mac1 and Mac3 (cyan) and the peroxisomal
84 marker protein mCherry-SKL (magenta) were inspected by epifluorescence microscopy. Representative images
85 of glucose grown cells (A) or oleate grown cells (B). Full images are shown as overlays of the green and red
86 channel. For insets single channels and merged channels are depicted. (C) Quantifications show Pearson's
87 correlation coefficients of GFP and mCherry signals for indicated strains. (D) Representative epifluorescence
88 image of cells expressing mCherry-Mac3 together with GFP-SKL organized as described above. (E) GFP-SKL
89 and mCherry-SKL or GFP-Mac3 and mCherry-Mac3 were co-expressed and representative images are shown
90 organized as described above. (F) Quantification show Pearson's correlation coefficients of GFP and mCherry
91 signals for indicated strains. (A); (B); (D) and (E) Scale bars: 5 µm.

92 Green fluorescent protein (GFP) tagged Mac1 or Mac3 showed only partial colocalization with
93 the red fluorescent peroxisomal reporter mCherry-SKL (Fig. 1A). Oleic acid is known to induce
94 peroxisome proliferation in various species including *U. maydis* (Camões et al., 2015;
95 Kohlwein et al., 2013). Four hours of incubation in oleic acid-containing medium substantially
96 enhanced the observed subpopulation phenotype (Fig. 1B). Quantifications revealed low
97 correlation coefficients for the red and the green signal (Figs. 1C, S1A and S1B). Reciprocal
98 exchange of fluorescent tags did not alter our results indicating that it was not the specific
99 fluorescent protein, which caused the remarkable enrichment in peroxisome subpopulations
100 (Fig. 1D). As a control, we expressed either the combination of GFP-Mac3 and mCherry-Mac3
101 or the combination of GFP-SKL and mCherry-SKL and observed a high degree of co-
102 localization (Fig. 1E). In aggregate these data show that both acyltransferases are localized only
103 in a fraction of peroxisomes suggesting that in *U. maydis* specific populations of peroxisomes
104 with different protein content exist.
105
106 **Accumulation of Mac1 and Mac3 inside of a subdomain of peroxisomes**
107 GFP-Mac1 or GFP-Mac3 fluorescence seemed not to fill the entire peroxisome but was
108 enriched in distinct foci that merged with only a section of the organelle stained by mCherry-
109 SKL (e.g. Fig. 1B). Therefore, we analyzed suborganellar localization of GFP-Mac1 and GFP-
110 Mac3 by super-resolution imaging using structured illumination microscopy (SIM)
111 (Gustafsson, 2000). Analysis of SIM images revealed that both fusion proteins indeed
112 concentrate in subdomains of peroxisomes, while mCherry-SKL and GFP-SKL were
113 distributed among the whole organelle (Fig. 2A to 2C). This was as well visualized by 3D-
114 reconstructions (Fig. 2D). Time-lapse imaging showed that foci containing acyltransferases are
115 stable over time (Fig. S2A and Movie 1).
116 Previous studies of mammalian peroxisomes uncovered a paracrystalline core region, which
117 typically contains the enzyme urate oxidase as a major constituent but also harbors additional
118 proteins (De Duve & Baudhuin, 1966; Völkl *et al*, 1988). We determined the localization of the
119 putative *U. maydis* urate oxidase ortholog (UMAG_00672) fused to GFP (GFP-Uox1). GFP-
120 Uox1 accumulated in foci similar to GFP-Mac1 and GFP-Mac3 and also occurred only in a
121 subpopulation of peroxisomes (Fig. 2E) suggesting that all three proteins are enriched in
122 structures probably representing the paracrystalline core of peroxisomes. Indeed, co-expression
123 of GFP-Uox1 and mCherry-Mac1 or GFP-Uox1 and mCherry-Mac3 resulted in a high degree
124 of colocalization (Fig. 2E and Fig. S2B).

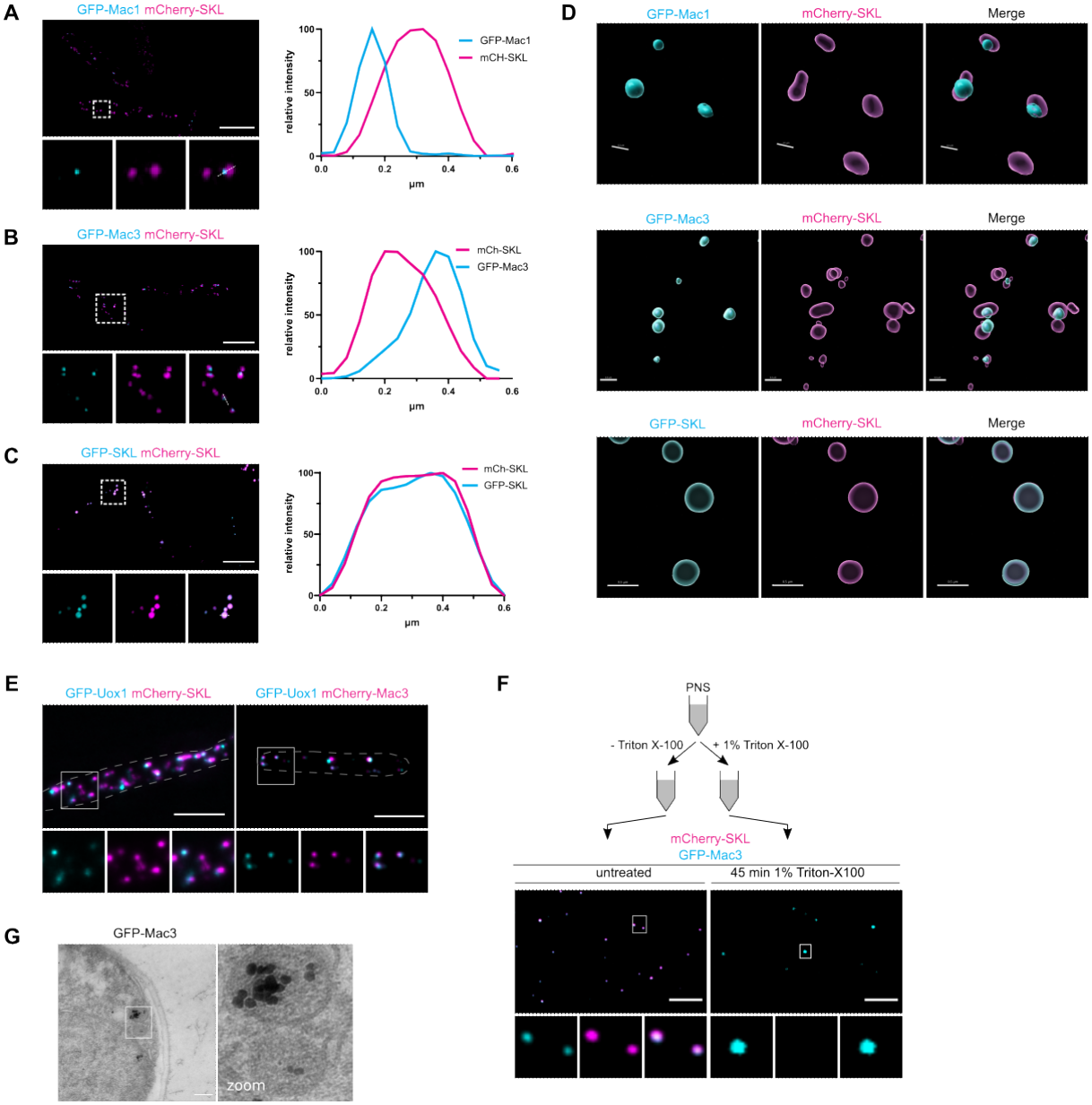

Figure 2 Acyltransferases Mac1 and Mac3 accumulate in peroxisome subdomains also enriched for urate oxidase Uox1.
Cells were analyzed by super-resolution microscopy using SIM. Representative images of cells expressing GFP-Mac1 and mCherry-SKL (A), GFP-Mac3 and mCherry-SKL (B) and GFP-SKL and mCherry-SKL (C). Full images are shown as overlays of the green and red channel. For insets single channels and merged channels are depicted. Associated graphs show the normalized fluorescence intensity of GFP and mCherry along the indicated lines. (D) 3D-reconstruction of GFP-Mac3 containing peroxisomal subdomains (cyan). Scale bar: 0.5 µm (E) Representative epifluorescence images of cells expressing GFP-Uox1 with mCherry-SKL (left) or mCherry-Mac3 (right). Organization of pictures as described above. Scale bars: 5 µm. (F) Crude organelle preparations of indicated strains were imaged by epifluorescence microscopy after incubation in lysis buffer supplemented with Triton X-100 (right). Preparations incubated in lysis buffer without Triton X-100 served as control (left). Organization of pictures as described above. Scale bars: 5 µm. (A) – (F) Signals of GFP-tagged proteins are shown in cyan and of mCherry-tagged proteins in magenta. (G) Transmission electron micrograph of cells expressing GFP-Mac3. Staining was achieved through labeling of GFP-Mac3 with anti-GFP and subsequent immunogold labeling followed by silver enhancement. Scale bar: 0.2 µm.

It was reported previously that the paracrystalline core of peroxisomes can sustain treatment with nonionic detergent (Tsukada et al., 1966). We prepared crude organelle extracts from

145 strains expressing mCherry-SKL together with GFP-Mac3, mCherry-Mac3 together with GFP-
146 Uox1 or mCherry-Mac1 together with GFP-Mac3. Triton X-100-treated or non-treated samples
147 were inspected by epifluorescence microscopy. While detection of mCherry-SKL was highly
148 sensitive to treatment with detergent, fluorescently labelled Mac1, Mac3 and Uox1 remained
149 visible inside of detergent resistant punctate structures (Fig. 2F and Fig. S2C). Furthermore,
150 transmission electron microscopy in combination with immunogold labeling showed that GFP-
151 Mac3 is concentrated within a subdomain of peroxisomes (Fig. 2G). Hence, foci enriched for
152 all three enzymes are structures that likely represent the paracrystalline core of *U. maydis*
153 peroxisomes.
154
155 **A short peptide motif sufficient for enrichment of proteins inside of the core region**
156 The C-terminal 12 amino acids contribute to targeting efficiency of PTS1 proteins (Brocard and
157 Hartig, 2006). To examine whether information within the peroxisomal targeting signal is
158 involved in formation of subdomains and subpopulations, we analyzed the localization of GFP
159 fused to the C-terminal PTS1 containing dodecamers of Mac1 and Mac3 (GFP-PTS1$_{Mac1}$ and
160 GFP-PTS1$_{Mac3}$) (Fig. 3A). Interestingly, only GFP-PTS1$_{Mac3}$ accumulated in subpopulations
161 and was enriched inside of peroxisomal foci, while GFP-PTS1$_{Mac1}$ colocalized with mCherry-
162 SKL positive peroxisomes and was homogenously distributed within the organelle (Fig. 3B
163 and 3C). By truncation analysis we identified a short peptide motif inside of the 12mer derived
164 from Mac3 consisting of the amino acid stretch Tyr-Ile-Ile-Val (TIIV) as required for efficient
165 focal accumulation of GFP (Fig. S3A and S3B). Insertion of this sequence motif between GFP
166 and a canonical SKL containing PTS1 motif induced enrichment of GFP inside of
167 subpopulations of peroxisomes (Fig. 3D). Fusion of the TIIV-tetrapeptide to the C-terminus of
168 a PTS2-GFP reporter protein (Ast et al., 2022) resulted in a similar pattern of localization (Fig.
169 3E and 3F). This suggests, that focal accumulation does not involve a specific pathway for
170 protein import but probably requires events that occur within the organelle.
171 To address if a TIIV motif does provoke subdomain formation in a different cellular
172 compartment or if it only functions inside of peroxisomes we attached it to the C-terminus of a
173 mitochondrial reporter protein containing an N-terminal mitochondrial targeting signal. This
174 chimeric fusion protein was detected inside of mitochondria in distinct foci suggesting that the
175 TIIV peptide triggers subdomain formation independent of the targeted organelle (Fig. 3G).

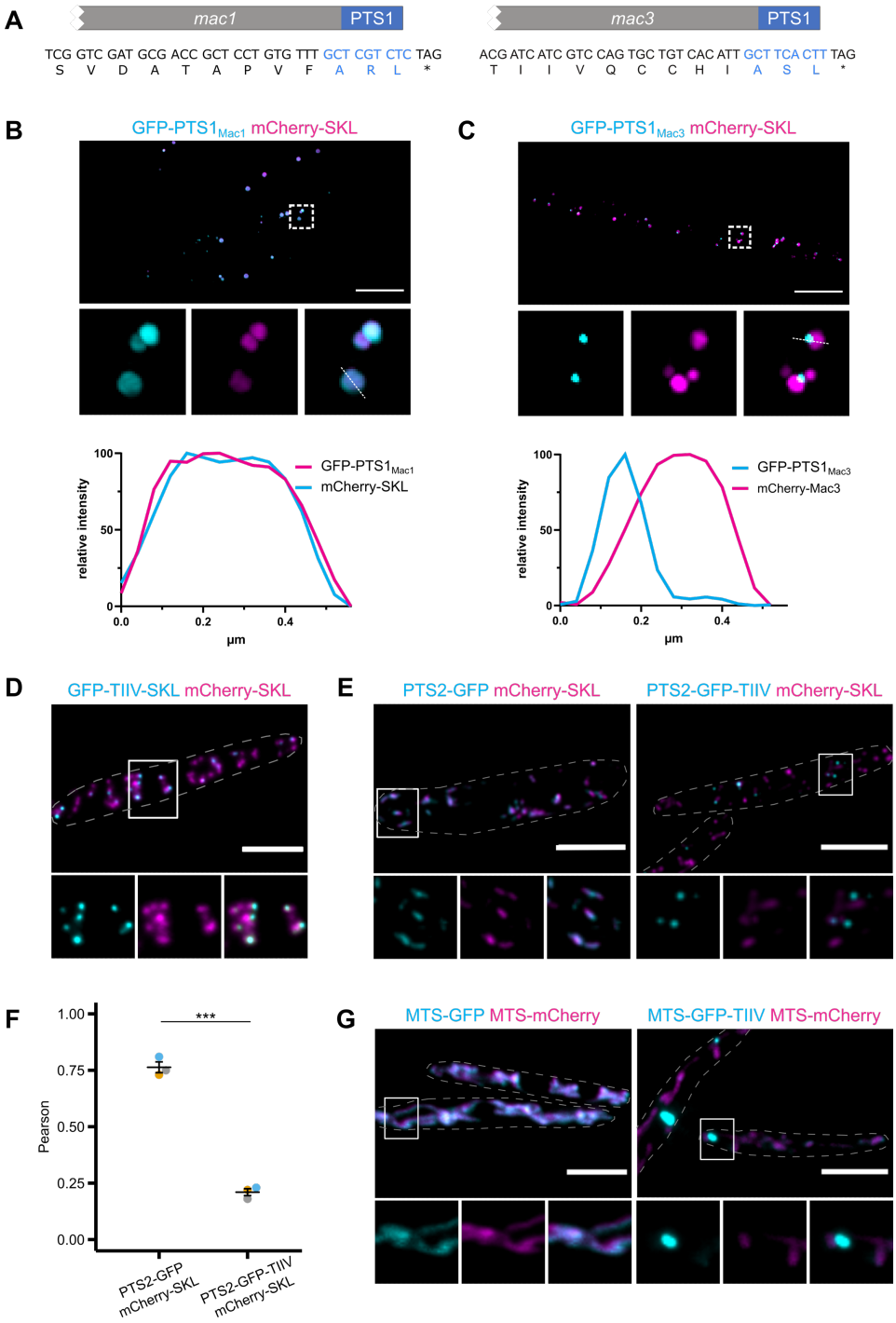

Figure 3 A short peptide motif sufficient for accumulation of proteins inside the core structure
(A) C-terminal dodecamers of Mac1 and Mac3 containing the characteristic PTS1 motifs. Cells were analyzed by super-resolution microscopy using SIM. Representative images of cells expressing GFP-PTS1$_{Mac1}$ and mCherry-SKL (B) or GFP-PTS1$_{Mac3}$ and mCherry-SKL. (C) Full images are shown as overlays of the green and red channel. For insets single channels and merged channels are depicted. Associated graphs show the normalized fluorescence intensity of GFP and mCherry along the indicated lines. (D) GFP fused to a peptide consisting of the small motif Tyr-Ile-Ile-Val (TIIV) and the prototype PTS1 Ser-Lys-Leu (SKL) was co-expressed with mCherry-SKL. A representative epifluorescence image is shown. Organization of the picture as above. (E) Cells expressing a PTS2-GFP reporter proteins either with or without a C-terminal TIIV motif were co-expressed with mCherry-SKL. Representative epifluorescence images are shown. Organization of the pictures as above. (F) Quantification show Pearson's correlation coefficients of GFP and mCherry signals for indicated strains. (G) GFP containing a mitochondrial targeting signal (MTS) either with or without an additional C-terminal TIIV motif was co-expressed with a MTS-mCherry. Representative epifluorescence images are shown. Organization of the pictures as above. ((A) – (E) and (G) Signals of GFP-tagged proteins are shown in cyan and of mCherry-tagged proteins in magenta. Scale bars: 5 µm.

192 **Identification of additional proteins enriched in the core structure**

193 Intrigued by the identification of a short peptide motif that triggers concentration of GFP inside
194 of intraperoxisomal foci we asked whether this could help uncovering additional protein
195 residents of the peroxisomal core structure.

196

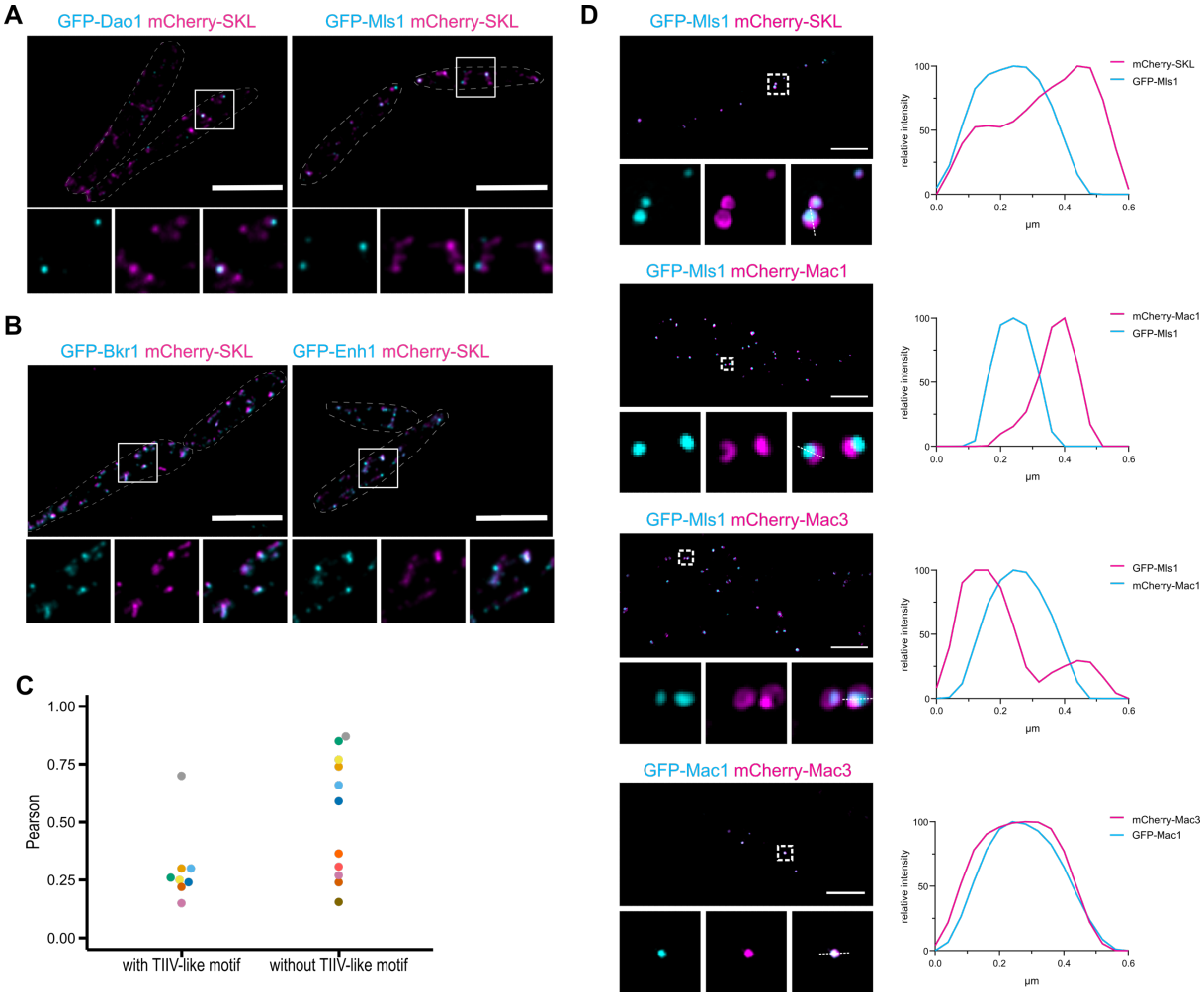

197

198 **Figure 4 Identification of additional PTS1 proteins enriched in the peroxisomal core structure**
199 (A) Two candidate proteins containing TIIV-like motifs – D-amino oxidase 1 (Dao1) and malate synthase 1 (Mls1)
200 – were co-expressed with mCherry-SKL. Representative epifluorescence images are shown. Full images are
201 provided as overlays of the green and red channel. For insets single channels and merged channels are depicted.
202 (B) Two candidate proteins without TIIV-like motif – a putative NADPH dependent beta-ketoacyl reductase
203 (Bkr1) and a putative enoyl-CoA hydratase (Enh1) – were co-expressed with mCherry-SKL. Representative
204 epifluorescence images are shown. (C) Quantification shows the mean value of Pearson's correlation coefficients
205 of GFP signals (candidate proteins) and mCherry-Signal signals (mCherry-SKL). Quantifications for three
206 replicates for each of the analyzed candidate proteins are shown in Fig. S4. (D) Co-localization of indicated fusion
207 protein was analyzed by SIM. Organization of pictures as above. Associated graphs show the normalized
208 fluorescence intensity of GFP and mCherry along the indicated lines.
209 (A, B and D) Signals of GFP-tagged proteins are shown in cyan and of mCherry-tagged proteins in magenta. Scale
210 bars: 5 µm.

211

212 We mined the predicted *U. maydis* proteome for candidates, which contain a TIIV motif or a
213 similar sequence in combination with a PTS1 (Tab. S1). We tested seven full-length candidate
214 proteins fused to GFP. Localization of six candidates resembled the so far identified proteins

215 Mac1, Mac3 and Uox1. The GFP signal accumulated within peroxisomal foci and in organelle
216 subpopulations (Fig. 4A and 4C; Fig. S4A). This strengthens our notion that the TIIV-like
217 motifs are involved in concentrating proteins into the core structure. Proteins from a control set
218 of randomly chosen PTS1-containing proteins that lack a TIIV-like motif on average showed a
219 higher co-localization with mCherry-SKL (Fig. 4B and 4C, Fig. S4B). The variability of
220 correlation coefficients, however, suggests that other features in the proteins contribute focal
221 enrichment in the core structure and formation of subpopulations as well.
222 Together, these data demonstrate that a significant number of peroxisomal matrix proteins
223 accumulates in peroxisomal foci. Other proteins have no or minor affinity to these structures or
224 are unable to form them (Fig. 4). The variable ability of proteins to form or accumulate in
225 subdomains likely represents a basic regulatory principle, which determines the luminal
226 distribution of peroxisomal matrix proteins. Among the enriched proteins were enzymes
227 involved in different metabolic pathways. These include the predicted D-amino oxidase Dao1
228 (UMAG_05703) and the malate synthase Mls1 (UMAG_15004) involved in glyoxylate
229 metabolism (Fig. 4A). Both proteins are also typical residents of peroxisomes in other
230 organisms (Kunze and Hartig, 2013; Pollegioni et al., 2007), but are not necessarily connected
231 in a metabolic network. Accordingly, enrichment of a particular protein does not coincide with
232 a specific peroxisomal pathway, but rather seems to be a feature shared by peroxisomal proteins
233 with very different biochemical functions. Interestingly, although Mac1, Mac3 and Mls1 are
234 detected in overlapping peroxisomal subdomains and enrich in similar subpopulations they
235 appear to be concentrated inside of different regions of the structures and may even exclude
236 each other to some extent (Fig. 4D), suggesting internal heterogeneity and a complex intrinsic
237 organization of the core structures.
238
239 **Peroxisome subpopulations form over time**
240 Enrichment of proteins in peroxisomal subdomains could result in their asymmetric distribution
241 when peroxisomes divide. This may support the formation of peroxisome subpopulations. To
242 follow GFP-Mac3 localization over time, GFP-Mac3 was expressed under control of an
243 arabinose inducible and glucose repressible promoter (Brachmann et al., 2001). As a control,
244 GFP fused to acyl-CoA oxidase 1 (Aox1; UMAG_02208) was used. GFP-Aox1 was not
245 enriched inside of the core, but uniformly distributed among peroxisomes upon constitutive
246 expression (Fig. S5A). Induction of both GFP fusion proteins (GFP-Mac3 or GFP-Aox1) in
247 strains that also express mCherry-SKL, was accomplished through incubation in arabinose
248 containing medium (Fig. 5A).

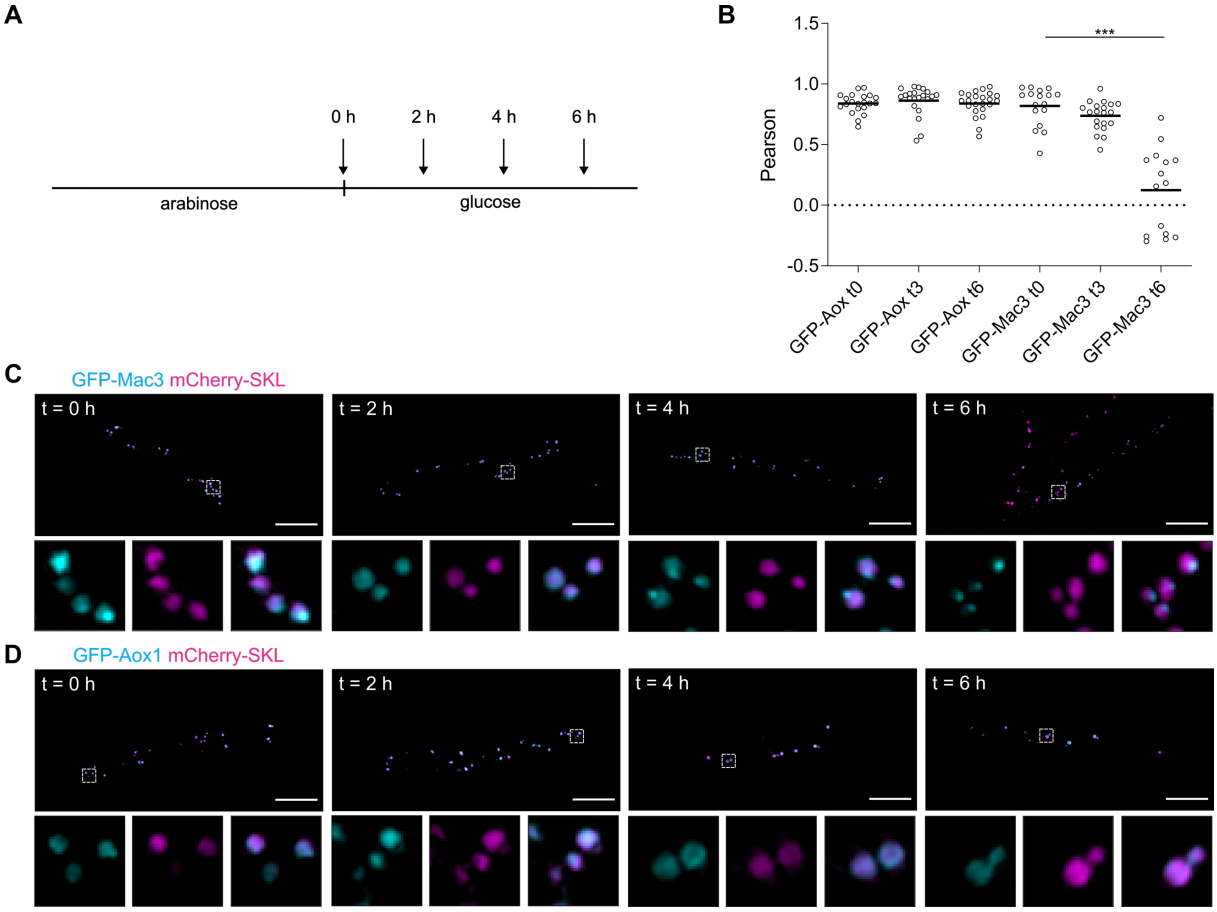

Figure 5 Accumulation in core structures and formation of subpopulations over time.
(A) Scheme of the transcriptional pulse-chase experiment to assess the formation of subdomains and subpopulations over time. Cells were incubated in arabinose medium for 2 hours to induce expression of GFP-tagged proteins. Expression was stopped via change to glucose containing medium. (B) Quantification of colocalization data derived from epifluorescence microscopy depicted in Fig. S5. Each circle represents one cell. (C and D). Cells were analyzed at indicated time points by super-resolution microscopy using SIM. GFP-Mac3 (C; cyan) was compared to GFP-Aox1 (D; cyan) – a protein not accumulating in the core structure upon constitutive expression (Fig. S5) – in strains containing mCherry-SKL (magenta). Full images are shown as overlays of the green and red channel. For insets single channels and merged channels are depicted.

After repression of gene expression by shifting cells to glucose medium we followed the localization of the fluorescent proteins at different time points by SIM and epifluorescence microscopy (Fig. 5A to 5D). Quantifications of epifluorescence images revealed that GFP-Mac3 containing subpopulations form over time (Fig. 5B and S5B). Both GFP-Mac3 and GFP-Aox1 were first uniformly distributed among peroxisomes (Fig. 5C and 5D). At later time points, GFP-Mac3, but not GFP-Aox1, accumulated in distinct foci within peroxisomes demonstrating formation of subdomains (Fig. 5C and 5D).

Specialization of peroxisome populations

270 We reasoned that the propensity of matrix proteins to self-assemble may control the protein
271 content of specialized peroxisomes. This is reminiscent to the biogenesis of peroxisome derived
272 Woronin bodies in filamentous ascomycetes (Jedd and Chua, 2000).
273

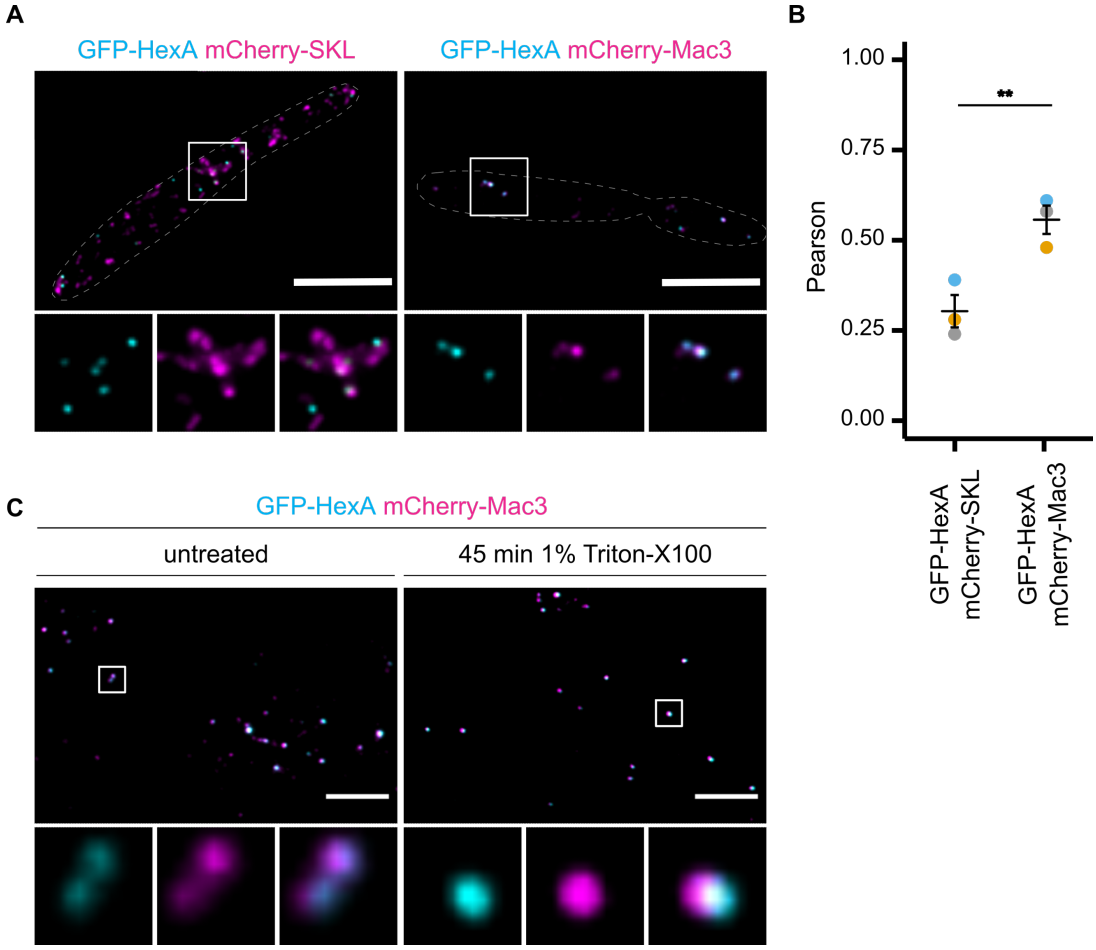

274
275
276 **Figure 6 The Woronin body protein HexA colocalizes with Mac3**
277 (A) *U. maydis* strains expressing an N-terminally GFP-tagged version of *A. nidulans* HexA (cyan) and mCherry-
278 SKL (magenta) or mCherry-Mac3 (magenta) were inspected by epifluorescence microscopy. Full images are
279 shown as overlays of the green and red channel. For insets single channels and merged channels are depicted. (B)
280 Quantification shows Pearson's correlation coefficients of GFP and mCherry signals for indicated strains. (C)
281 Crude organelle preparations of indicated strains were imaged by epifluorescence microscopy after incubation in
282 lysis buffer supplemented with Triton X-100 (right). Preparations incubated in lysis buffer without Triton X-100
283 served as control (left). Organization of pictures as described above.
284
285 These specialized peroxisome derived compartments are enriched in a protein dubbed Hex1 in
286 *N. crassa*, which forms crystalline structures resistant to detergent (Jedd and Chua, 2000; Liu
287 et al., 2011, 2008; Yuan et al., 2003). We hypothesized that subdomain formation in *U. maydis*
288 and Woronin body formation represent special adaptations of a more generic mechanism that
289 regulates formation of distinct peroxisome populations. We, therefore, fused GFP to the
290 *Aspergillus nidulans* Woronin body protein HexA (Momany et al., 2002; Zekert et al., 2010)
291 and co-expressed GFP-HexA in *U. maydis* together with either mCherry-Mac3 or mCherry-

292 SKL. mCherry-Mac3 and GFP-HexA were detected in highly overlapping foci whereas
293 mCherry-SKL and GFP-HexA showed a lower degree of co-localization (Figs. 6A and 6B).
294 mCherry-Mac3 and GFP-HexA also appeared in stable and overlapping structures following
295 treatment of crude organelle extracts with detergent (Fig. 6C). This data supports the concept
296 that formation of luminal peroxisomal subdomains in *U. maydis* and formation of Woronin
297 bodies in ascomycetes follows similar mechanistic principles.
298
299 **TIIV dependent accumulation in peroxisomal subdomains of mammalian cells**
300 Finally, we addressed transferability of our finding to a different biological system and
301 expressed GFP combined with a minimal PTS1 ending on SKL and containing the TIIV motif
302 in human retinal pigment epithelial 1 (RPE1) cells.
303

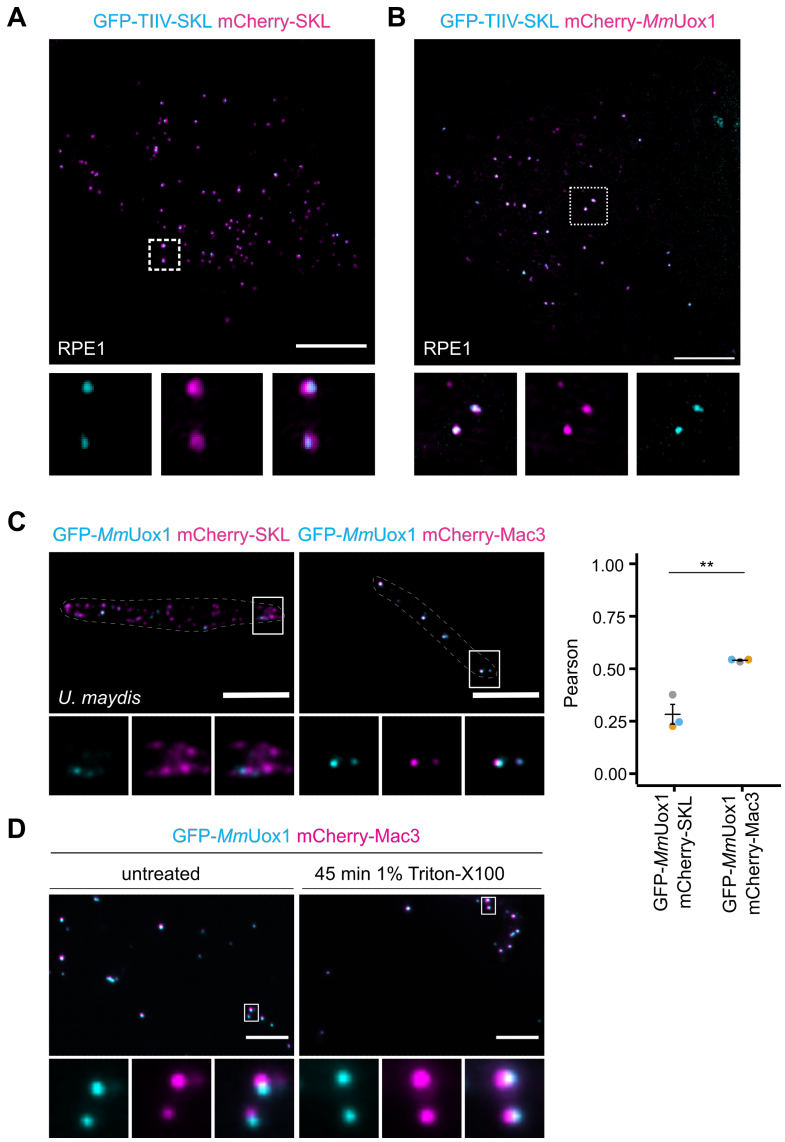

304
305

306 **Figure 7 Similar mechanistic principles for enrichment in the core of *U. maydis* and mammalian**
307 **peroxisomes**
308 (A) Constructs expressing GFP-TIIV-SKL and mCherry-SKL were transfected into RPE1 cells. Cells were
309 analyzed by SIM. The representative picture shows an overlay of the GFP-signal (cyan) and the mCherry-signal
310 (magenta) in the overview. The signal of single channels as well as the overlay are depicted for magnified insets.
311 (B) *Mus musculus* urate oxidase (*Mm*UOX1) was tagged with mCherry (magenta) and co-expressed with GFP-
312 TIIV-SKL (cyan) in RPE1 cells. Cells were analyzed by SIM. Representative pictures are organized as above. (C)
313 *M. musculus* urate oxidase (*Mm*UOX1) was tagged with GFP (cyan) and expressed in *U. maydis* cells either co-
314 expressing mCherry-SKL (magenta) or mCherry-Mac3 (magenta). Representative pictures are organized as above.
315 (D) Quantifications show Pearson's correlation coefficients of GFP and mCherry signals for indicated strains. (E)
316 Crude organelle preparations of indicated strains were imaged by epifluorescence microscopy after incubation in
317 lysis buffer supplemented with Triton X-100 (right). Preparations incubated in lysis buffer without Triton X-100
318 served as control (left). Organization of pictures as described above. Scale bars: 5 µm.
319
320 mCherry-SKL was again used as marker for peroxisomes and subcellular localization of
321 fluorescent proteins was analyzed by SIM. We obtained similar data as in *U. maydis* and
322 observed accumulation of GFP-TIIV-SKL in defined subdomains of peroxisomes in RPE1 cells
323 (Fig. 7A). To test if these structures are also enriched for a protein found in the native
324 paracrystalline core of mammalian peroxisomes we co-expressed GFP-TIIV-SKL together with
325 mCherry fused to murine urate oxidase 1 (*Mm*UOX1). GFP-TIIV-PTS1 showed a profound co-
326 localization with mCherry-*Mm*UOX1 revealing that both proteins are located in vicinity (Fig.
327 7B). Thus, the rules underlying protein concentration inside of the paracrystalline core are likely
328 similar in fungi and in humans. To further confirm this theory we performed complementary
329 experiments in *U. maydis* cells and expressed GFP fused to murine *Mm*UOX1 together with
330 either mCherry-SKL or mCherry-Mac3. Again, we detected a higher degree of overlap for GFP-
331 UOX1 and mCherry-Mac3 than for GFP-*Mm*UOX1 and mCherry-SKL (Fig. 7C). In addition,
332 we could observe stability of GFP-*Mm*UOX1 containing structures upon detergent treatment of
333 crude organelle extracts (Fig. 7D). Both results are consistent with our model, that in diverse
334 eukaryotic species formation of the core structure of peroxisomes follows analogous principles
335 and is a major driving force to spatially organize the peroxisomal proteome.
336
337 **Discussion**
338 Here, we have shown selective accumulation of various proteins in subdomains of peroxisomes
339 likely identical to the paracrystalline core structure. This process turned out as a driving force
340 for the generation of organelle subpopulations with different protein content. Remarkably,
341 independent of the original organism or biochemical function all so far tested proteins enriched
342 in these structures show a high degree of co-localization in *U. maydis* and in human cells (Figs.
343 1 – 4, Fig. 7). Even the very specialized protein HexA from *A. nidulans* exhibited a very similar
344 pattern of localization suggesting that selective enrichment of this peculiar peroxisomal protein

345 required for Woronin body biogenesis (Jedd & Chua, 2000) follows parallel mechanistic
346 principles (Fig. 6).
347 The variable ability to self-assemble inside of the lumen of the peroxisome may be a
348 fundamental principle to determine the proteome of every single peroxisome. Peroxisomes
349 proliferate by fission, constantly divide but in contrast to other organelles may not regularly
350 fuse at least in their mature form (Islinger et al., 2012). Thus, the asymmetric segregation of the
351 core will lead to peroxisome subpopulations with different protein content after any fission
352 event. Combined with altered protein expression levels this will almost certainly derive many
353 unique peroxisome variants within a single cell. Furthermore, peroxisomes can accumulate
354 huge amounts of cargo protein (DeLoache et al., 2016; Grewal et al., 2021) and the ability of
355 proteins to accumulate in the core structure may be one prerequisite or even a catalyzer.
356 Peroxisomes are attractive organelles for implantation of synthetic pathways (DeLoache &
357 Dueber, 2013; Simon et al., 2020; Stehlik et al., 2014). Forced concentration of enzymes by
358 addition of TIIV-like motifs might be another way to optimize or to modulate these pathways.
359 Protein crystallization for structural determination purposes (Schönherr et al., 2018) might
360 benefit from our finding as well.
361 Our data provide first insights into a novel code, which will evolve our understanding of the
362 spatial organization of the peroxisomal proteome. The identification of sequence motifs
363 sufficient for focal accumulation is a starting point to systematically deduce structural
364 differences between proteins that tend to exhibit a homogenous luminal peroxisomal
365 distribution or reside in peroxisomal subdomains. The core structure is, most probably,
366 metabolically active as it is a major site of a number of abundant enzymes including catalase,
367 urate oxidase or alcohol oxidase of methylotrophic yeasts (Hayashi et al., 1976; Veenhuis et
368 al., 1981; Völkl et al., 1988; Heinze et al., 2000; Schönherr et al., 2018). Given the surprising
369 variability of proteins with the ability to enrich in this structure (Fig. 3), its internal organization
370 is of considerable interest. Can proteins go in and out regularly? Are their different layers of
371 enrichment for particular proteins as indicated by our data for acyltransferases and malate
372 synthase 1 from *U. maydis* (Fig. 4)? Is there biochemical activity everywhere in the core? The
373 process of formation may even exhibit functional parallels with phase separation of proteins
374 (Boeynaems et al., 2018; Hyman et al., 2014).
375 In summary, our work contributes to a more detailed characterization of a conserved
376 peroxisomal structure, which is known since the discovery of the peroxisome (De Duve &
377 Baudhuin, 1966; Rouiller & Bernhard, 1956) but whose formation and composition has not
378 been addressed in greater detail until now.

379 **Methods**

380 **Microorganism, growth conditions and transformation**

381 *Escherichia coli* strain TOP10 (Invitrogen) was used for all cloning purposes and amplification
382 of plasmid DNA. *U. maydis* strains generated and used in this study are derivatives of Bub8,
383 MB215 and Bub8 mCherry-SKL (Freitag et al., 2012; Hewald et al., 2005; Weinzierl et al.,
384 2002) and listed in Supplementary Table 2 (Tab. S2). All strains are available from the authors
385 upon reasonable request. *U. maydis* cells were grown at 28°C in YEPSlight medium (Tsukuda
386 et al., 1988) or yeast nitrogen base medium (YNB; Difco) supplemented either with 2% glucose
387 and 0.2% ammonium sulfate or 0.2% oleic acid (Roth), 0.1% Tween-40 and 0.2% ammonium
388 sulfate at pH 5.6. For epifluorescence imaging cells were grown in oleic acid media if not
389 specified differently. SIM imaging was performed on glucose grown cells to circumvent artifact
390 of oleic acid addition. For chase experiments (Fig. 5) *U. maydis* cells were grown overnight in
391 YEPSlight medium. Subsequently, cells were washed and diluted in YNB medium containing
392 2% arabinose and 0.2% ammonium sulfate and incubated for 2 h. Expression of fusion proteins
393 was stopped by shifting the cells to YNB medium containing 2% glucose and 0.2 % ammonium
394 sulfate cells and the localization of the fluorescent proteins was microscopically monitored at
395 indicated time points. Cell transformation was performed as previously described (Hanahan et
396 al., 1991; Schulz et al., 1990). DNA was integrated into the *ip*-locus of *U. maydis* cells
397 (Broomfield & Hargreaves, 1992) or randomly integrated into the genome. Hygromycin (200
398 µg/ml), carboxin (2 µg/ml) and G418 (400 µg/ml) were used for selection. Genomic DNA was
399 extracted as previously described (Hoffman and Winston, 1987).

400

401 **Human cell line and transient transfection of cells**

402 hTert-RPE1 cells (ATCC CRL-4000) were cultured in DMEM-F12 medium (Life
403 Technologies) supplemented with 10% FCS and Penicillin/Streptomycin (100 U/mL penicillin,
404 100 µg/mL streptomycin) at 37°C, 5% CO2. Cells were transiently transfected with the help of
405 Fugene 6 (Promega) using a ratio of 3:1 of reagent to DNA. Cells were transfected in MatTek
406 3.5 cm glass-bottom dishes. 12 h after transfection, the medium was replaced to remove
407 transfection reagent, and the cells were imaged between 16 h and 20 h post transfection.

408

409 **Molecular cloning and nucleic acid procedures**

410 Standard procedures were followed for plasmid generation (Sambrook et al., 1989). Plasmids
411 used for protein expression in *U. maydis* are derivatives of the plasmids pOTEF-GFP-Ala6-
412 MMXN and pCRG-GFP-Ala6-MXN (Böhmer et al., 2008). Plasmids used for expression of

413 fluorescent proteins in hTert-RPE1 cells are derivatives of the plasmid pEGFP-C1 and
414 pmCherry-C1 (Clontech). Plasmids were analyzed by sequencing. All plasmids and
415 oligonucleotides used in this study are listed in Supplementary table S2 (Tab. S2). Plasmids are
416 available from the authors upon reasonable request.
417
418 **Epifluorescence microscopy**
419 Logarithmically grown *U. maydis* cells were treated with 100 µM Carbonyl cyanide m-
420 chlorophenyl hydrazine (CCCP) resolved in dimethyl sulfoxide to block peroxisomal
421 movement. For the majority of experiments using epifluorescence microscopy cells were
422 incubated in oleic acid-containing media for four hours prior to imaging experiments as
423 formation of subpopulations was easier to follow under these conditions (exceptions: imaging
424 experiments underlying Figs. 1A and S5). After 5-10 minutes incubation at room temperature,
425 the cells were either placed on 1% agarose cushions containing 100 µM Carbonyl cyanide m-
426 chlorophenyl hydrazine CCCP on a microscope glass slide and covered with a coverslip or
427 placed on MatTek 3.5 cm glas-bottom dishes and covered with an 1% agarose cushion
428 containing 100 µM CCCP as well. For time-lapse imaging no CCCP was added.
429 Epifluorescence microscopy was performed on an Axiovert 200 M inverse microscope (Zeiss)
430 equipped with a 1394 ORCA ERA CCD camera (Hamamatsu Photonics), filter sets for eGFP
431 and rhodamine, and a Zeiss 63x Plan Apochromat oil lens (NA 1.4). The software Volocity 5.3
432 (Perkin-Elmer) was used for image acquisition. The ImageJ plugin DeconvolutionLab with 25
433 iterations of the Richardson-Lucy algorithm was used for image deconvolution (Vonesch and
434 Unser, 2008), point-spread functions for each channel were computed by the ImageJ plugin
435 PSF Generator using the Richards & Wolf model (Kirshner et al., 2013). Alternatively,
436 epifluorescence microscopy as well as time-lapse experiments (500 ms time-lapse for 60 s)
437 were performed on a Deltavision OMX V4 microscope (GE Healthcare) equipped with three
438 water-cooled PCO edges CMOS cameras, a solid-state light source and a laser-based autofocus.
439 The software softWoRx (Applied Precision, GE Healthcare) was used for image deconvolution.
440 Images were processed in ImageJ/Fiji (Schneider et al., 2012).
441
442 **SIM**
443 Three-dimensional structured illumination microscopy (SIM) was performed on a Deltavision
444 OMX V4 microscope with and Olympus x60 NA 1.42 objective and three PCO.edge sCMOS
445 cameras and 488 nm and 568 nm laser lines. Cells were illuminated with a grid pattern. 15 raw
446 images (3 orientations, 5 phases) were taken for each image plane. SoftWoRx software

447 (Applied Precision, GE Healthcare) was used for image reconstruction, alignment and
448 projection. Images were processed in ImageJ/Fiji (Schneider et al., 2012). For 3D visualization
449 of peroxisomal subdomains, surfaces were generated using Imaris.
450
451 **Transmission electron microscopy and Immunogold labelling**
452 For visualization of *U. maydis* cells expressing GFP-Mac3 using transmission electron
453 microscopy (TEM) 50 ml logarithmically growing cells were harvested and frozen under high-
454 pressure (Wohlwend HPF Compact 02). After subsequent freeze substitution (using acetone,
455 containing 0.25% osmium tetroxide, 0.2% uranyl acetate, 0.05% ruthenium red, and 5% water)
456 (Leica AFS2), cells were embedded in Epon812 substitute resin (Fluka). Embedded cells were
457 sectioned to 50 nm thin sections (Leica EM UC7 RT), which were used for immunolabeling
458 with α-GFP (Rockland; dilution 1:500). As a secondary antibody rabbit-anti-goat antibodies
459 coupled to ultra-small gold particles were used (Aurion, dilution 1:100). Subsequently a silver
460 enhancement procedure was performed and sections were post-stained with 2% uranyl acetate
461 and 0.5% lead citrate. Analysis of the samples was conducted with a JEOL JEM2100 TEM
462 equipped with a fast-scan 2k CCD TVIPS (Gauting, Germany) F214 camera. Images were
463 processed with ImageJ (Schneider et al., 2012).
464
465 **Preparation of crude organelles**
466 Preparation of post-nuclear supernatants was adapted from previous protocols (Cramer et al.,
467 2015; Kremp et al., 2020; Stehlik et al., 2020). Briefly, 200 ml of logarithmically growing cells
468 were harvested for 5 min at 1600 x g at 23°C. Cells were washed two times with deionized
469 water and two times with sorbitol buffer (1.2 M sorbitol; 20 mM KH_2PO_4 adjusted to pH 7.4
470 with K_2HPO_4). Formation of spheroplasts was achieved through incubation in sorbitol buffer
471 containing novozyme (4µg/ml) for 30 – 45 min. Degradation of the cell wall was followed
472 microscopically. Afterwards, spheroplasts were kept on ice and gently washed two times with
473 sorbitol buffer – centrifugation for 10 min at 2300 rpm at 4°C. Spheroplasts were gently washed
474 with lysis buffer (5 mM MES, 0.5 mM EDTA, 1 mM KCl, 0.6 M Sorbitol, 1 mM 4-
475 aminobenzamidine dihydrochloride, 1 µg/ml aprotinin, 1 µg/ml leupeptin, 1 mM
476 phenylmethylsulfonyl fluoride, 10 µg/ml N-tosyl-L-phenylalanine chloromethyl ketone, and 1
477 µg/ml pepstatin) – centrifugation for 10 min at 2300 rpm at 4°C, resuspended in 15 ml lysis
478 buffer and frozen at -80°C overnight. Homogenization was achieved through 2 x 10 strokes
479 with a Potter-Elvehjem homogenizer interrupted by chilling the samples on ice for 2 min.

480 Nuclei and cell debris were removed by two subsequent centrifugations at 1600 × g for 10 min.
481 Subsequently, the PNS was diluted to an OD600 of 1, aliquoted and frozen at -80°C.
482
483 **Detergent treatment**
484 PNS fractions were thawed on ice, centrifuged at 10k*g for 10 min at 4°C and concentrated
485 10x in lysis buffer. Samples were split into halves and aliquots were incubated in lysis buffer
486 containing 1% Triton-X-100 or in lysis buffer for 45 min. Preparations were immediately
487 analyzed by epifluorescence microscopy immobilized on 1% agarose cushions.
488
489 **Quantification of peroxisomal subpopulations and statistical analysis**
490 Microscopic data was collected from at least three independent *U. maydis* cultures (biological
491 replicates) for each experiment. At least five images per culture with at least ten cells were
492 quantified. Quantification of co-localization was performed as follows. Detection and
493 measurement of individual peroxisomes was performed automatically via an ImageJ macro
494 (Supplementary File 1). Briefly, maximum projections of deconvolved RFP and GFP z-stacks
495 were created, transformed into 16-bit images and corrected for channel-misalignment by the
496 "StackReg 2.0.0" plugin using "Rigid Body" transformation (Thevenaz et al., 1998;
497 https://sites.imagej.net/BIG-EPFL/plugins/) to later serve as the reference images for detection
498 of peroxisomes; same operations were performed on average projections of the respective non-
499 deconvolved z-stacks for later fluorescence-intensity measurements. To increase sensitivity and
500 account for peroxisomes showing only fluorescence in one of the two channels, the resulting
501 images were merged using the Image Calculator function with the maximum option (detection
502 based on only RFP or GFP references was still included in the macro but performed less reliable
503 than using the merge of both references). For detection of peroxisomes, the merged average
504 projections were used to create a mask of the cells. This mask was used to determine the
505 background noise outside of the cells in the reference merge. The resulting maximum noise
506 intensity was used for the Find Maxima function of ImageJ; individual peroxisomes were
507 detected in the reference merge and marked as point selections. These selections were restored
508 in the background-corrected average projections of the non-deconvolved stacks of both
509 channels. Subsequently, circular ROIs of a 3-pixel radius (area of 32 pixels) were created
510 around the point selections and signal intensities were measured for both channels (as Raw
511 Integrated Density per ROI) and stored side-by-side in the results file for the whole dataset. A
512 commented version of the macro is attached to the manuscript. For evaluation of the resulting
513 data, the statistics software R was used (R Core Team, 2015): measured intensities were

514 normalized to one and a linear regression analysis was performed with the RFP intensities as
515 independent and GFP intensities as dependent variable, in addition a correlation test was
516 performed (Pearson's). Superplots (Lord et al., 2020) and statistical tests were computed using
517 RStudio 1.2.1335 with R 3.6.0 or GraphPadPrism. Plots are structured as follows: center line,
518 mean; error bars, standard error of the mean; circles, mean of experiments. P-values were
519 calculated using an unpaired, two-sided Student's t-test using Graphpad Prism. For data
520 depicted in Fig. 1 and Fig. S3C, which contain multiple comparisons a 1-Way anova combined
521 with a Tukeys post-test was performed to assess significance of the differences. * refers to a p-
522 value lower than or equal to 0.05; ** refer to a p-value lower than or equal to 0.01 and ***lower
523 than or equal to 0.001. ****lower than 0.0001. The graph shown in Fig. 5 was generated using
524 Graphpad Prism. Each dot represents one cell.
525
526 **Bioinformatics and accession numbers**
527 *U. maydis* putative peroxisomal PTS1 protein sequences were retrieved from the *Ustilago*
528 *maydis* genome database (MUMDB) or broad institute and manipulated with notepad ++ using
529 regular expressions (regex). PTS1 motifs were bookmarked with the regular expression
530 '([SA][RKHQNS][LI]|[SA][RK][MFV]|[PCVGE][RK][LI])*$'. Protein sequences containing
531 a TIIV-like motif were bookmarked with the regular expression '(T [I, L, V] [I, L, V] [I, L, V]
532 [I, L, V] [I, L, V])*$'. Peroxisomal candidate proteins with TIIV-like motif and without motif
533 were randomly chosen and the localization of the peroxisomal proteins to subdomains was
534 analyzed by fluorescence microscopy. All genes can now be accessed via the National Center
535 of Biotechnology Information (NCBI) via the UMAG number.
536
537 **Data availability**
538 Any supporting original data for this study can be requested from the corresponding authors.
539
540 **Acknowledgments**
541 We thank Marisa Piscator and Ulrikke Dahl Brinch for excellent technical assistance. We are
542 grateful to Reinhard Fischer and Valentin Wernet for plasmids. JA was supported by a
543 fellowship from Marburg Research Academy. TS acknowledges funding from SYNMIKRO.
544 KS was supported by a Career grant from the South-Eastern Norway Regional Health Authority
545 (2020038) and a Research Grant from the Research Council of Norway (315103). JF
546 acknowledges funding from the DFG (grant ID FR-3586/2-1).
547

Author contributions

Conceptualization: JA, DM, KS and JF; Data acquisition: JA, NB, DM, TH, BS, KS and JF. Preparation of figures: JA, NB, DM and KS; Generation of code, bioinformatic and statistical analysis: JA, NB, TS, CR, KS; Supervision: CT, GB, MB, KS, JF; Writing – original draft: JF; Writing – revision and editing: All authors. Analysis of data: All authors.

553 Ast J, Bäcker N, Bittner E, Martorana D, Ahmad H, Bölker M, Freitag J. 2022. Two Pex5 Proteins With
554 Different Cargo Specificity Are Critical for Peroxisome Function in Ustilago maydis. *Front Cell Dev Biol*
555 **10**. doi:10.3389/fcell.2022.858084
556 Bartoszewska M, Opalinski L., Veenhuis M, van der Klei IJ. 2011. The significance of peroxisomes in
557 secondary metabolite biosynthesis in filamentous fungi. *Biotechnol Lett* **33**:1921–1931.
558 Baudhuin P, Beaufay H, de Duve C. 1965. Combined biochemical and morphological study of particulate
559 fractions from rat liver : Analysis of Preparations Enriched in Lysosomes or in Particles Containing Urate
560 Oxidase, D-Amino Acid Oxidase, and Catalase . *J Cell Biol* **26**:219–243. doi:10.1083/jcb.26.1.219
561 Becker F, Stehlik T, Linne U, Bölker M, Freitag J, Sandrock B. 2021. Engineering *Ustilago maydis* for
562 production of tailor-made mannosylerythritol lipids. *Metab Eng Commun* **12**:e00165.
563 doi:https://doi.org/10.1016/j.mec.2021.e00165
564 Boeynaems S, Alberti S, Fawzi NL, Mittag T, Polymenidou M, Rousseau F, Schymkowitz J, Shorter J, Wolozin
565 B, Van Den Bosch L, others. 2018. Protein phase separation: a new phase in cell biology. *Trends Cell Biol*
566 **28**:420–435.
567 Böhmer C, Böhmer M, Bölker M, Sandrock B. 2008. Cdc42 and the Ste20-like kinase Don3 act independently
568 in triggering cytokinesis in *Ustilago maydis*. *J Cell Sci* **121**:143–148.
569 Bölker M, Basse CW, Schirawski J. 2008. *Ustilago maydis* secondary metabolism—From genomics to
570 biochemistry. *Fungal Genet Biol* **45**:S88--S93.
571 Bortfeld M, Auffarth K, Kahmann R, Basse CW. 2004. The *Ustilago maydis* a2 mating-type locus genes *lga2*
572 and *rga2* compromise pathogenicity in the absence of the mitochondrial p32 family protein Mrb1. *Plant*
573 *Cell* **16**:2233-48.
574 Brachmann A, Weinzierl G, Kämper J, Kahmann R. 2001. Identification of genes in the bW/bE regulatory
575 cascade in *Ustilago maydis*. *Mol Microbiol* **42**:1047–1063.
576 Brocard C, Hartig A. 2006. Peroxisome targeting signal 1: is it really a simple tripeptide? *Biochim Biophys Acta*
577 **1763**:1565–73. doi:10.1016/j.bbamcr.2006.08.022
578 Broomfield PLE, Hargreaves JA. 1992. A single amino-acid change in the iron-sulphur protein subunit of
579 succinate dehydrogenase confers resistance to carboxin in Ustilago maydis. *Curr Genet* **22**:117–121.
580 Camões F, Islinger M, Guimarães SC, Kilaru S, Schuster M, Godinho LF, Steinberg G, Schrader M. 2015. New
581 insights into the peroxisomal protein inventory: Acyl-CoA oxidases and-dehydrogenases are an ancient
582 feature of peroxisomes. *Biochim Biophys Acta (BBA)-Molecular Cell Res* **1853**:111–125.
583 Cramer J, Effelsberg D, Girzalsky W, Erdmann R. 2015. Small-scale purification of peroxisomes for analytical
584 applications. *Cold Spring Harb Protoc*. doi:10.1101/pdb.prot083717
585 De Duve C. 1960. Intracellular Localization of Enzymes. *Nature* **187**:836. doi:10.1038/187836a0
586 De Duve C, Baudhuin P. 1966. Peroxisomes (microbodies and related particles). *Physiol Rev* **46**:323–357.
587 DeLoache WC, Dueber JE. 2013. Compartmentalizing metabolic pathways in organelles. *Nat Biotechnol*
588 **31**:320–321.
589 DeLoache WC, Russ ZN, Dueber JE. 2016. Towards repurposing the yeast peroxisome for compartmentalizing
590 heterologous metabolic pathways. *Nat Commun* **7**:11152. doi:10.1038/ncomms11152
591 Francisco T, Rodrigues TA, Dias AF, Barros-Barbosa A, Bicho D, Azevedo JE. 2017. Protein transport into
592 peroxisomes: knowns and unknowns. *BioEssays* **39**:1700047.
593 Freitag J, Ast J, Bölker M. 2012. Cryptic peroxisomal targeting via alternative splicing and stop codon read-

through in fungi. *Nature* **485**:522–525.

Freitag J, Ast J, Linne U, Stehlik T, Martorana D, Bölker M, Sandrock B. 2014. Peroxisomes contribute to biosynthesis of extracellular glycolipids in fungi. *Mol Microbiol* **93**:24–36.

Galiani S, Waithe D, Reglinski K, Cruz-Zaragoza LD, Garcia E, Clausen MP, Schliebs W, Erdmann R, Eggeling C. 2016. Super resolution microscopy reveals compartmentalization of peroxisomal membrane proteins. *J Biol Chem* jbc--M116.

Gould SJ, Keller GA, Hosken N, Wilkinson J, Subramani S. 1989. A conserved tripeptide sorts proteins to peroxisomes. *J Cell Biol* **108**:1657–1664.

Grewal PS, Samson JA, Baker JJ, Choi B, Dueber JE. 2021. Peroxisome compartmentalization of a toxic enzyme improves alkaloid production. *Nat Chem Biol* **17**:96–103.

Gründlinger M, Yasmin S, Lechner BE, Geley S, Schrettl M, Hynes M, Haas H. 2013. Fungal siderophore biosynthesis is partially localized in peroxisomes. *Mol Microbiol*. **88(5):**862-75

Gustafsson MGL. 2000. Surpassing the lateral resolution limit by a factor of two using structured illumination microscopy. *J Microsc* **198**:82–87.

Hanahan D, Jessee J, Bloom FR. 1991. Plasmid transformation of Escherichia coli and other bacteria. *Methods Enzymol* **204**:63–113.

Hayashi H, Taya K, Suga T, Niinobe S. 1976. Studies on Peroxisomes. VI. Relationship between the Peroxisomal Core and Urate Oxidase1. *J Biochem* **79**:1029–1034. doi:10.1093/oxfordjournals.jbchem.a131143

Heinze M, Reichelt R, Kleff S, Eising R. 2000. High Resolution Scanning Electron Microscopy of Protein Inclusions (Cores) purified from Peroxisomes of Sunflower (Helianthus annuus L.) Cotyledons. *Cryst Res Technol* **35**:877–886. doi:https://doi.org/10.1002/1521-4079(200007)35:6/7<877::AID-CRAT877>3.0.CO;2-S

Hewald S, Josephs K, Bölker M. 2005. Genetic analysis of biosurfactant production in Ustilago maydis. *Appl Environ Microbiol* **71**:3033–3040.

Hoffman CS, Winston F. 1987. A ten-minute DNA preparation from yeast efficiently releases autonomous plasmids for transformaion of *Escherichia coli*. *Gene* **57**:267–272.

Hu J, Baker A, Bartel B, Linka N, Mullen RT, Reumann S, Zolman BK. 2012. Plant peroxisomes: biogenesis and function. *Plant Cell* **24**:2279–2303.

Hyman AA, Weber CA, Jülicher F. 2014. Liquid-liquid phase separation in biology. *Annu Rev Cell Dev Biol*. doi:10.1146/annurev-cellbio-100913-013325

Islinger M, Grille S, Fahimi HD, Schrader M. 2012. The peroxisome: an update on mysteries. *Histochem Cell Biol* **137**:547–574.

Jedd G, Chua NH. 2000. A new self-assembled peroxisomal vesicle required for efficient resealing of the plasma membrane. *Nat Cell Biol* **2**:226–231.

Kämper J, Kahmann R, Bölker M, Ma LJ, Brefort T, Saville BJ, Banuett F, Kronstad JW, Gold SE, Müller O, others. 2006. Insights from the genome of the biotrophic fungal plant pathogen *Ustilago maydis*. *Nature* **444**:97–101.

Kim PK, Hettema EH. 2015. Multiple pathways for protein transport to peroxisomes. *J Mol Biol* **427**:1176–1190.

Kohlwein SD, Veenhuis M, van der Klei IJ. 2013. Lipid Droplets and Peroxisomes: Key Players in Cellular

Lipid Homeostasis or A Matter of Fat—Store'em Up or Burn'em Down. *Genetics* **193**:1–50.

Kremp M, Bittner E, Martorana D, Klingenberger A, Stehlik T, Bölker M, Freitag J. 2020. Non-AUG Translation Initiation Generates Peroxisomal Isoforms of 6-Phosphogluconate Dehydrogenase in Fungi. *Front Cell Dev Biol* **8**:251. doi:10.3389/fcell.2020.00251

Kumar S, de Boer R, van der Klei IJ. 2018. Yeast cells contain a heterogeneous population of peroxisomes that segregate asymmetrically during cell division. *J Cell Sci* **131**:jcs207522.

Kunze M, Hartig A. 2013. Permeability of the peroxisomal membrane: lessons from the glyoxylate cycle. *Front Physiol* **4**:204.

Lazarow PB. 2006. The import receptor Pex7p and the PTS2 targeting sequence. *Biochim Biophys Acta (BBA)-Molecular Cell Res* **1763**:1599–1604.

Lingard MJ, Monroe-Augustus M, Bartel B. 2009. Peroxisome-associated matrix protein degradation in Arabidopsis. *Proc Natl Acad Sci U S A*. doi:10.1073/pnas.0811329106

Liu F, Lu Y, Pieuchot L, Dhavale T, Jedd G. 2011. Import oligomers induce positive feedback to promote peroxisome differentiation and control organelle abundance. *Dev Cell*. doi:10.1016/j.devcel.2011.08.004

Liu F, Ng SK, Lu Y, Low W, Lai J, Jedd G. 2008. Making two organelles from one: Woronin body biogenesis by peroxisomal protein sorting. *J Cell Biol* **180**:325–339.

Lord SJ, Velle KB, Mullins RD, Fritz-Laylin LK. 2020. SuperPlots: Communicating reproducibility and variability in cell biology. *J Cell Biol* **219**. doi:10.1083/jcb.202001064

Momany M, Richardson EA, Van Sickle C, Jedd G. 2002. Mapping Woronin body position in *Aspergillus nidulans*. *Mycologia* **94**:260–266.

Nguyen TA, Le S, Lee M, Fan J-S, Yang D, Yan J, Jedd G. 2021. Fungal Wound Healing through Instantaneous Protoplasmic Gelation. *Curr Biol* **31**:271-282.e5.

Pieuchot L, Jedd G. 2012. Peroxisome assembly and functional diversity in eukaryotic microorganisms. *Annu Rev Microbiol* **66**:237–263.

Poirier Y, Antonenkov VD, Glumoff T, Hiltunen JK. 2006. Peroxisomal β-oxidation—a metabolic pathway with multiple functions. *Biochim Biophys Acta* **1763**:1413–1426.

Pollegioni L, Piubelli L, Sacchi S, Pilone MS, Molla G. 2007. Physiological functions of D-amino acid oxidases: from yeast to humans. *Cell Mol Life Sci* **64**:1373–1394. doi:10.1007/s00018-007-6558-4

Rouiller C and Bernhard W. 1956 "Microbodies" and the problem of mitochondrial regeneration in liver cells. J Biophys Biochem Cytol Suppl. 2: 355-359.

Sambrook J, Fritsch EF, Maniatis T. 1989. Molecular Cloning: A Laboratory Manual, Cold Spring Harbor Laboratory, Molecular Cloning a laboratory manual. Cold Spring Harbor Laboratory Press. doi:10.1128/AEM.71.8.4602

Schneider CA, Rasband WS, Eliceiri KW. 2012. NIH Image to ImageJ: 25 years of image analysis. *Nat Methods*. doi:10.1038/nmeth.2089

Schönherr R, Rudolph JM, Redecke L. 2018. Protein crystallization in living cells. *Biol Chem* **399**:751–772. doi:doi:10.1515/hsz-2018-0158

Schulz B, Banuett F, Dahl M, Schlesinger R, Schäfer W, Martin T, Herskowitz I, Kahmann R. 1990. The b alleles of *U. maydis*, whose combinations program pathogenic development, code for polypeptides containing a homeodomain-related motif. *Cell* **60**:295–306.

Simon D, Thomas WW, Yixuan L, Codruta I, C. KS. 2020. Transforming yeast peroxisomes into microfactories

676 for the efficient production of high-value isoprenoids. *Proc Natl Acad Sci* **117**:31789–31799.
677 doi:10.1073/pnas.2013968117
678 Smith JJ, Aitchison JD. 2013. Peroxisomes take shape. *Nat Rev Mol Cell Biol* **14**:803–817.
679 Stehlik T, Kremp M, Kahnt J, Bölker M, Freitag J. 2020. Peroxisomal targeting of a protein phosphatase type 2C
680 via mitochondrial transit. *Nat Commun* **11**:2355. doi:10.1038/s41467-020-16146-3
681 Stehlik T, Sandrock B, Ast J, Freitag J. 2014. Fungal peroxisomes as biosynthetic organelles. *Curr Opin*
682 *Microbiol* **22**:8–14. doi:http://dx.doi.org/10.1016/j.mib.2014.09.011
683 Tey WK, North AJ, Reyes JL, Lu YF, Jedd G. 2005. Polarized Gene Expression Determines Woronin Body
684 Formation at the Leading Edge of the Fungal Colony. *Mol Biol Cell* **16**:2651–2659.
685 Thevenaz P, Ruttimann UE, Unser M. 1998. A pyramid approach to subpixel registration based on intensity.
686 *IEEE Trans Image Process* **7**:27–41. doi:10.1109/83.650848
687 Tsukada H, Mochizuki Y, Fujiwara S. 1966. The nucleoids of rat liver cell microbodies fine structure and
688 enzymes. *J Cell Biol* **28**:449–460.
689 Tsukuda T, Carleton S, Fotheringham S, Holloman WK. 1988. Isolation and characterization of an
690 autonomously replicating sequence from Ustilago maydis. *Mol Cell Biol* **8**:3703–3709.
691 van der Klei IJ, Veenhuis M. 2006. Yeast and filamentous fungi as model organisms in microbody research.
692 *Biochim Biophys Acta* **1763**:1364–1373.
693 Veenhuis M, Harder W, van Dijken JP, Mayer F. 1981. Substructure of crystalline peroxisomes in methanol-
694 grown Hansenula polymorpha: evidence for an in vivo crystal of alcohol oxidase. *Mol Cell Biol* **1**:949–
695 957.
696 Völkl A, Baumgart E, Fahimi HD. 1988. Localization of urate oxidase in the crystalline cores of rat liver
697 peroxisomes by immunocytochemistry and immunoblotting. *J Histochem \& Cytochem* **36**:329–336.
698 doi:10.1177/36.4.3346536
699 Völkl A, Mohr H, Fahimi H. D. 1999. Peroxisome Subpopulations of the Rat Liver: Isolation by Immune Free
700 Flow Electrophoresis. *J Histochem Cytochem* **47**:1111–1117. doi:10.1177/002215549904700902
701 Walter T, Erdmann R. 2019. Current Advances in Protein Import into Peroxisomes. *Protein J* **38**:351–362.
702 doi:10.1007/s10930-019-09835-6
703 Wanders RJA. 2014. Metabolic functions of peroxisomes in health and disease. *Biochimie* **98**:36–44.
704 Weinzierl G, Leveleki L, Hassel A, Kost G, Wanner G, Bölker M. 2002. Regulation of cell separation in the
705 dimorphic fungus *Ustilago maydis*. *Mol Microbiol* **45**:219–231.
706 Yuan P, Jedd G, Kumaran D, Swaminathan S, Shio H, Hewitt D, Chua N-H, Swaminathan K. 2003. A HEX-1
707 crystal lattice required for Woronin body function in *Neurospora crassa*. *Nat Struct Mol Biol* **10**:264–270.
708 doi:10.1038/nsb910
709 Zekert N, Veith D, Fischer R. 2010. Interaction of the *Aspergillus nidulans* Microtubule-Organizing Center
710 (MTOC) Component ApsB with Gamma-Tubulin and Evidence for a Role of a Subclass of Peroxisomes in
711 the Formation of Septal MTOCs. *Eukaryot Cell* **9**:795–805. doi:10.1128/EC.00058-10

712 **Supplementary figures**

713

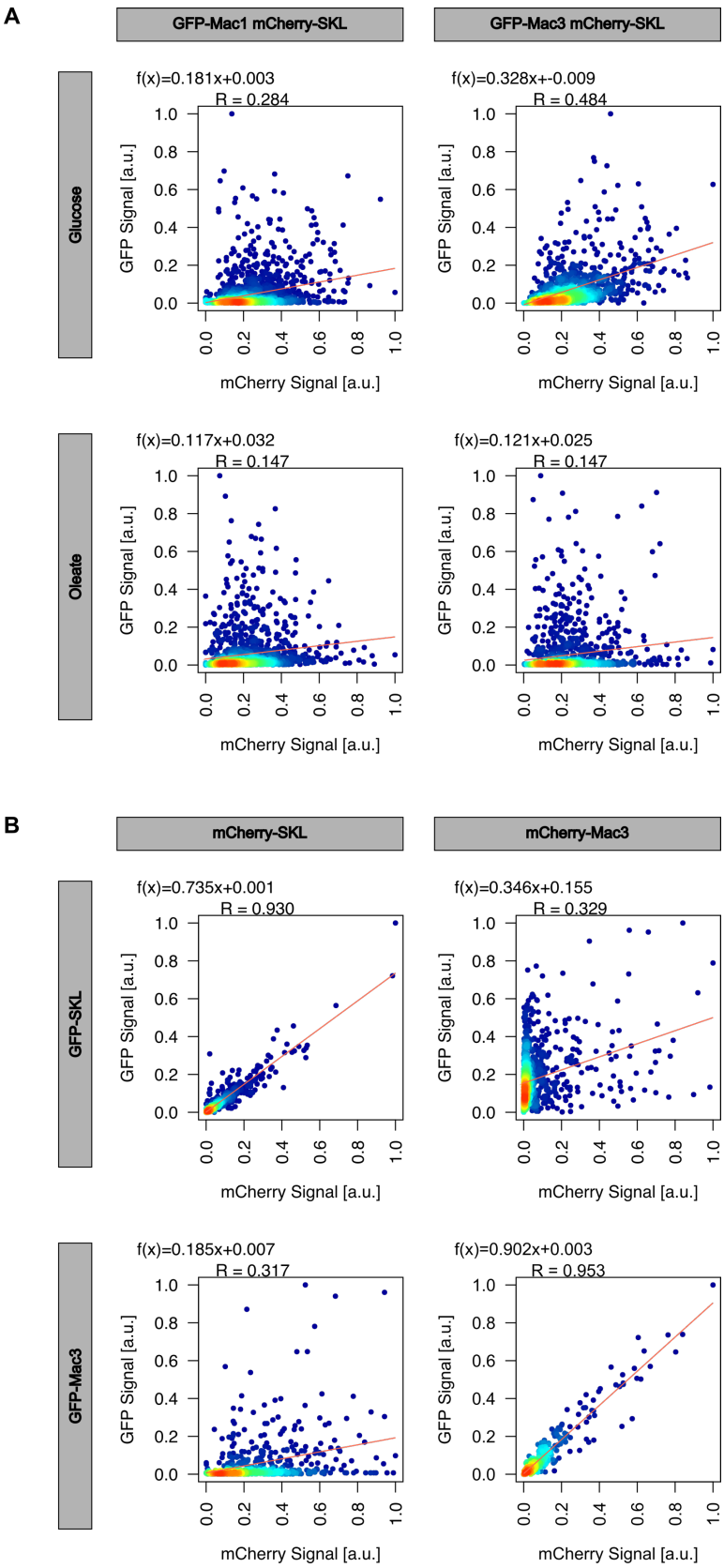

714

715 **Figure S1 Examples for the quantification of co-localization**
716 Representative plots showing the fluorescence signals of all analyzed peroxisomes in a representative replicate.
717 (A) related to Fig. 1C (B) related to Fig. 1F.

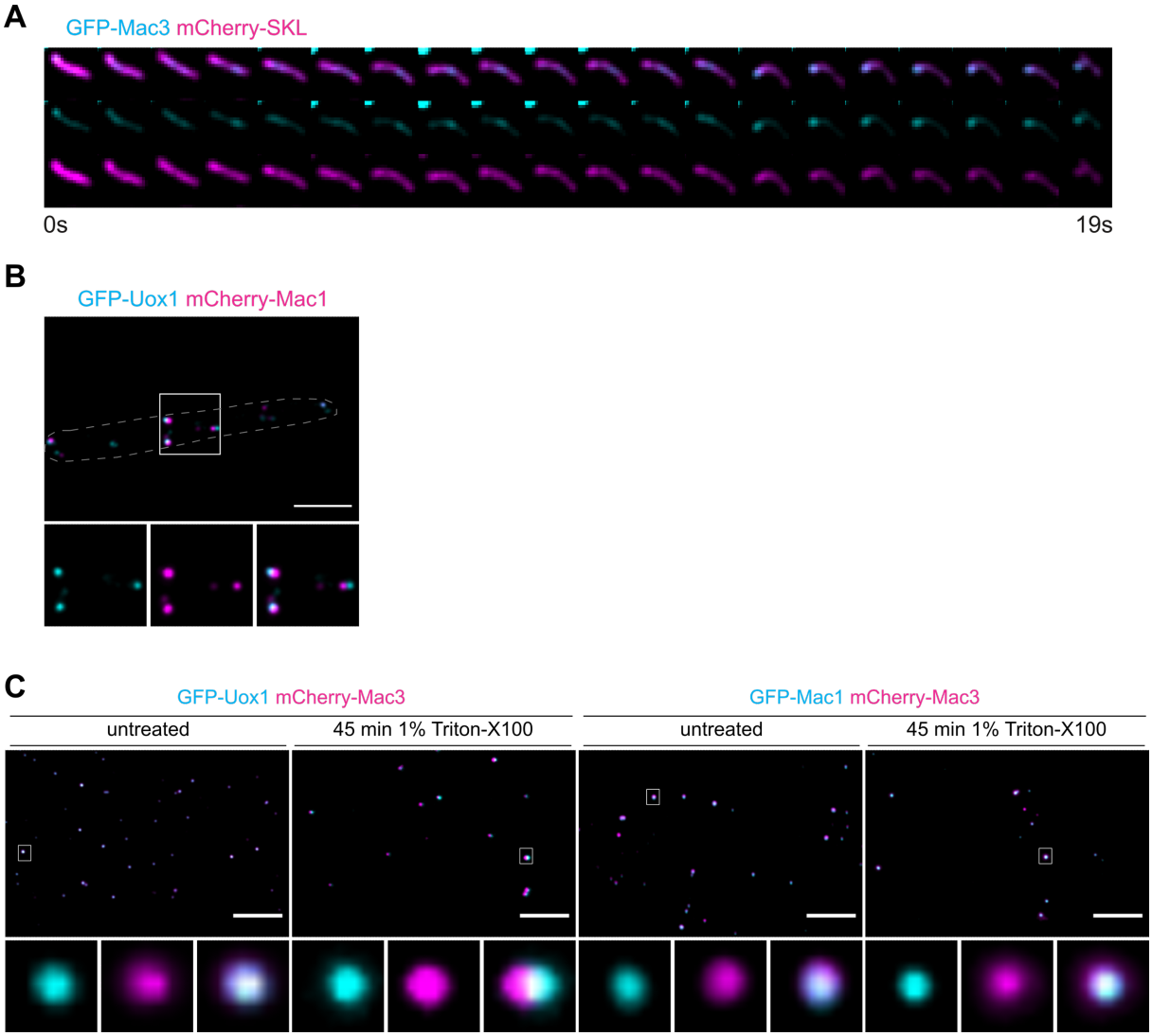

Figure S2 Mac proteins localize in detergent resistant peroxisomal subdomains also enriched for urate oxidase 1

(A) Time lapse imaging related to Movie 1. Epifluorescence imaging of GFP-Mac3 (cyan) and mCherry-SKL (magenta). One frame per second was recorded. Shown are overlays of the mCherry and GFP signal. (B) A representative image of cells expressing GFP-Uox1 and mCherry-Mac1. Full images are shown as overlays of the green and red channel. For insets single channels and merged channels are depicted. Scale bar: 5 µm. (C) Crude organelle preparations of indicated strains were imaged by epifluorescence microscopy after incubation in lysis buffer supplemented with Triton X-100 (right). Preparations incubated in lysis buffer without Triton X-100 served as control (left). Organization of pictures as described above. Scale bars: 5 µm.

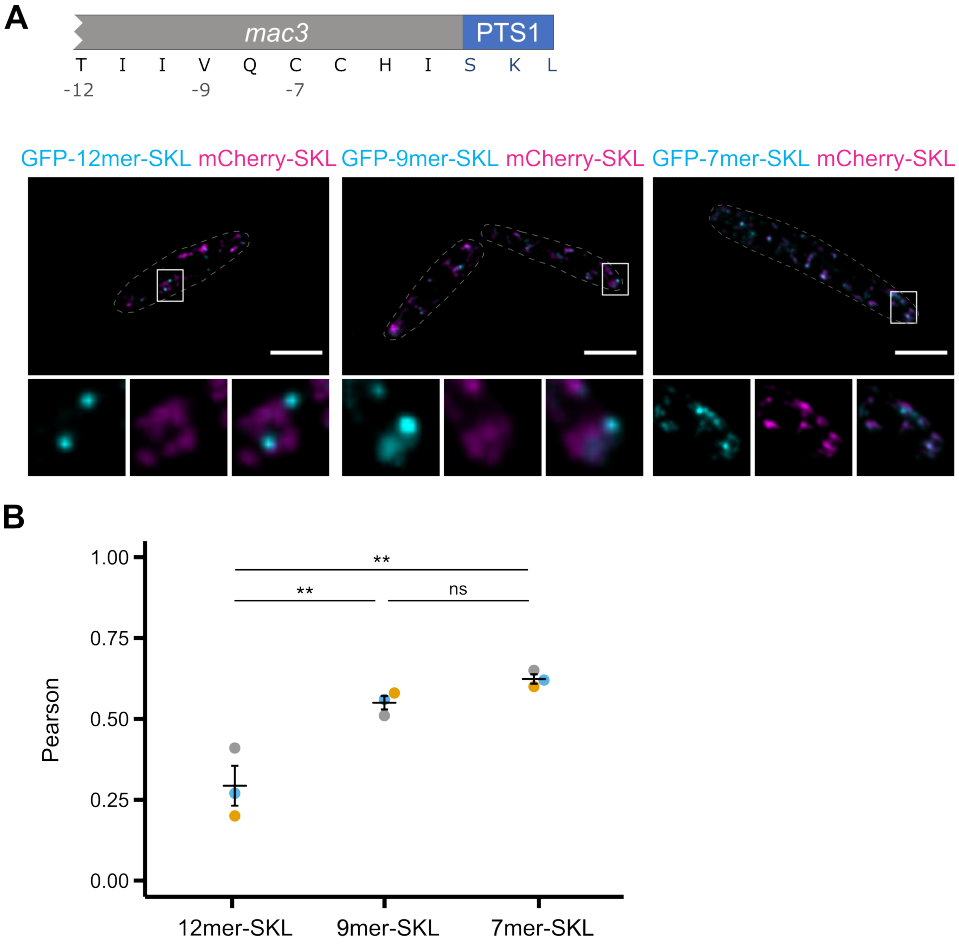

729

730

731 **Figure S3 Truncation analysis of the C-terminal dodecamer of Mac3**
732 (A) Depiction of the 3'end of the *mac3* gene encoding the peroxisomal targeting signal PTS1. Please note that the
733 unusual ASL motif had to be substituted by SKL to perform the subsequent truncation analysis as truncated
734 fragment of the dodecamer did not allow full peroxisomal import, which perturbs co-localization analysis (B)
735 Indicated fragments of the C-terminal dodecamer were fused to GFP (cyan) and analyzed in strains also expressing
736 mCherry-SKL (magenta). Full representative images are shown as overlays of the green and red channel. For
737 insets single channels and merged channels are depicted. Scale bars: 5 µm. (C) Quantification of co-localization
738 of experiments shown in (B).

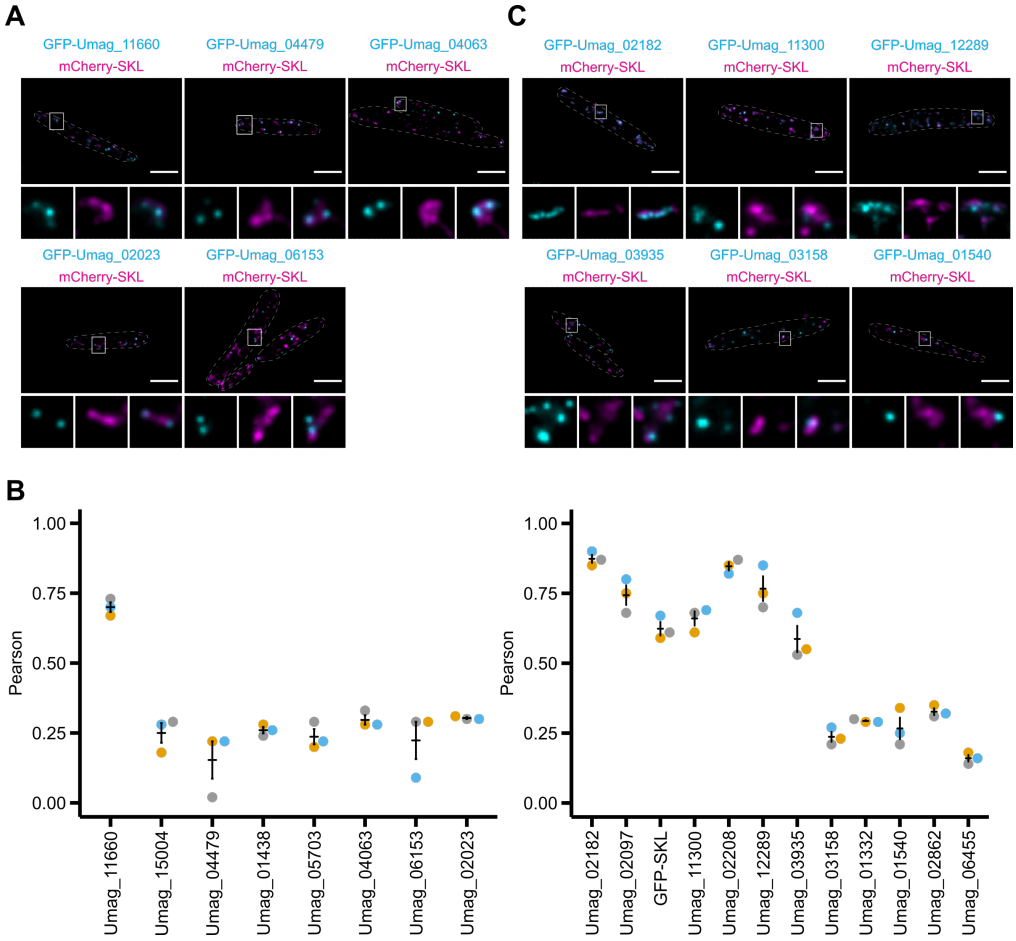

Figure S4 Analysis of candidate proteins with or without TIIV-like motif
U. maydis strains expressing N-terminally GFP-tagged versions of candidate proteins (cyan) with TIIV like motifs (A) or without TIIV-like motifs (C) and the peroxisomal marker protein mCherry-SKL (magenta) were inspected by epifluorescence microscopy. Full representative images are shown as overlays of the green and red channel. For insets single channels and merged channels are depicted. Scale bars: 5 µm. Umag numbers are gene identifiers accessible via NCBI. (B) Quantifications show Pearson's correlation coefficients of GFP and mCherry signals for indicated strains.

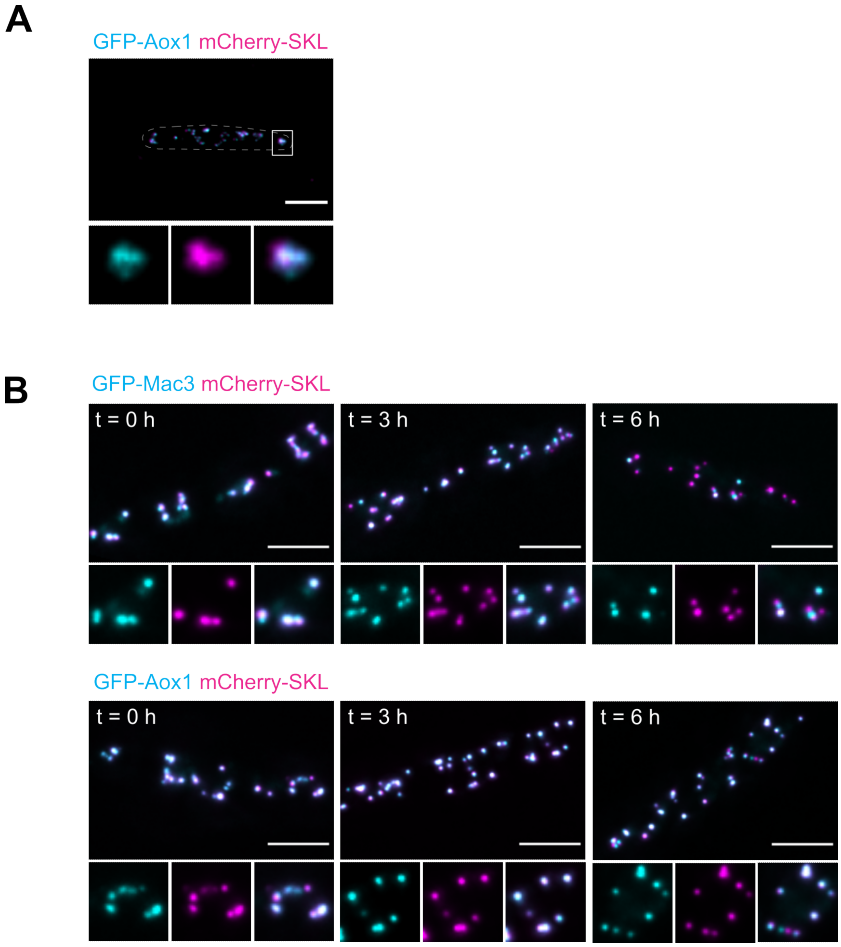

Fig. S5 Formation of peroxisome subpopulations over time.
(A) *U. maydis* strains expressing an N-terminally GFP-tagged version of Aox1 (cyan) and the peroxisomal marker protein mCherry-SKL (magenta) were inspected by epifluorescence microscopy. Full images are shown as overlays of the green and red channel. For insets single channels and merged channels are depicted. Scale bar: 5 µm. **(B)** Cells were analyzed at indicated time points after addition of glucose by epifluorescence microscopy. GFP-Mac3 (cyan) was compared to GFP-Aox1 (cyan) in strains containing mCherry-SKL (magenta). Full images are shown as overlays of the green and red channel. For insets single channels and merged channels are depicted. Quantifications of (B) are shown in Fig. 5.